

Investigation of long-term light stability of negative charge injected into oxide-nitride-oxide passivation stack of crystalline silicon solar cells

Cite as: J. Appl. Phys. **132**, 213302 (2022); doi: [10.1063/5.0111681](https://doi.org/10.1063/5.0111681)

Submitted: 19 July 2022 · Accepted: 10 November 2022 ·

Published Online: 1 December 2022



Christopher Chen,^{1,a)} Jeong-Mo Hwang,¹ Young-Woo Ok,² Wook-Jin Choi,² Vijaykumar Upadhyaya,² Brian Rounsaville,² and Ajeet Rohatgi²

AFFILIATIONS

¹Inert Plasma Charging LLC, Chandler, Arizona 85286, USA

²Georgia Institute of Technology, Atlanta, Georgia 30332, USA

^{a)}Author to whom correspondence should be addressed: christopher@plasmacharging.com

ABSTRACT

A negatively charged oxide-nitride-oxide stack for field-effect passivation of crystalline silicon solar cells is discussed. The negative charge was injected into the stack by a plasma charge injection technology. Charge stability was studied by exposing samples to AM1.5 simulation visible light and full-spectrum light at temperatures ranging from 55 to 78 °C for up to 300 h. Charge injection and loss were quantified based on shifts in the flatband voltage of capacitance–voltage curves measured with a mercury probe. The most probable mechanism of charge loss was found to be diffusion of negative charged hydrogen atoms through nitride and bottom oxide. The optimum recipe for each layer of the stack was investigated to minimize the loss of injected charge. The flatband voltage decay of the optimized stack was found to fit a power-law trend, suggesting the dispersive transport of hydrogen atoms with a dispersion parameter of ~ 0.06 – 0.07 . The optimized stack is projected to maintain a negative charge density of about $3.6 \times 10^{12} \text{ cm}^{-2}$ or more after 25 years of field operation in an environment such as Arizona, which would be sufficient for field-effect passivation under one-sun illumination. The high stability of the negative injected charge makes the plasma charging technology a safer and lower cost alternative to Al_2O_3 -passivation technology commonly used to passivate p-type surfaces.

Published under an exclusive license by AIP Publishing. <https://doi.org/10.1063/5.0111681>

I. INTRODUCTION

Effective surface passivation is a necessity for high-efficiency solar cells. The field effect passivation of p-type surfaces is typically accomplished using aluminum oxide (Al_2O_3) that contains a high density of negative fixed charges.¹ The accumulation layer formed by the negative charges repels minority carriers (electrons), preventing photo-generated carriers from surface recombination. However, the precursor material tri-methyl-aluminum (TMA) presents safety concerns which increases the expenses of working with Al_2O_3 technology.

Silicon nitride (SiN_x) films deposited by plasma-enhanced chemical vapor deposition (PECVD) are widely used in solar cells and are suitable for n-type surface passivation due to their positive fixed charge. However, if used to passivate p-type surfaces, the positive charge can induce an inversion layer that causes shunting and

degrades cell efficiency.² The introduction of a net negative charge in SiN_x films would avoid this degradation and allow for the replacement of the more complex and costly Al_2O_3 . We have successfully injected negative charge into SiN_x films using a plasma charge injection technology detailed in an earlier publication.³ Bifacial PERC cells fabricated using a negatively charged SiN_x rear passivation scheme have shown comparable efficiency to cells using Al_2O_3 rear passivation.⁴

A major concern that needs to be addressed for the adoption of plasma charging technology for commercial production is the stability of the injected charge in field operations. High ambient temperatures and strong sunlight are factors that could reduce the injected charge over time and, therefore, weaken the effect of the accumulation layer or field effect passivation.

To address this issue, we performed a series of light exposures on samples using a solar simulator. Capacitance–voltage (C–V)

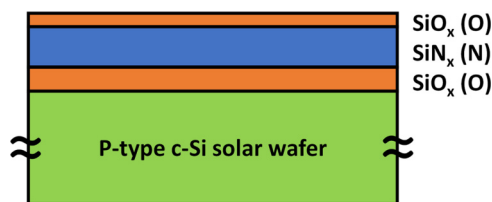


FIG. 1. Schematic cross section diagram for a solar test wafer with an ONO stack on one side for charge injection and charge stability tests.

measurements were used to estimate charge concentrations and the decay rate of injected charge. We have found that charge retention is drastically enhanced by changing the composition of SiN_x in an oxide/nitride/oxide dielectric stack.⁴ In this work, we have continued to investigate the effect of different compositions and processing conditions for silicon nitride and oxide layers on the charge decay rate. From the experimental results, we propose a likely mechanism of charge loss and present an optimized passivation stack that demonstrates the capability of plasma charge injection technology to provide sufficient charge for long-term operation of cells in the field.

II. EXPERIMENTS

For the purposes of charge injection and charge stability tests, an oxide/nitride/oxide (ONO) passivation stack was deposited on p-type Czochralski (Cz) silicon solar wafers with a resistivity of $\sim 1 \Omega \text{ cm}$. The wafers received nearly the same process flow as typical p-type PERC cells including high-temperature POCl_3 doping on the front side and high-temperature firing but excluding metal paste application on the rear side for charge stability tests and capacitance–voltage (C–V) measurements. KOH solutions were used for saw damage removal and texturing as well as rear surface planarization. A schematic of a typical test sample is shown in Fig. 1. The injected charge is stored in the silicon nitride (SiN_x) layer, while the oxides serve to confine the charge within the nitride. Several different batches of samples were prepared to isolate the effects of different processing conditions and materials for each layer on charge stability. From the results of these batches, an optimized batch was fabricated that minimizes the loss of injected charge.

The passivation stack was deposited on the substrate by a PECVD tool from Centrotherm operating at an RF frequency of

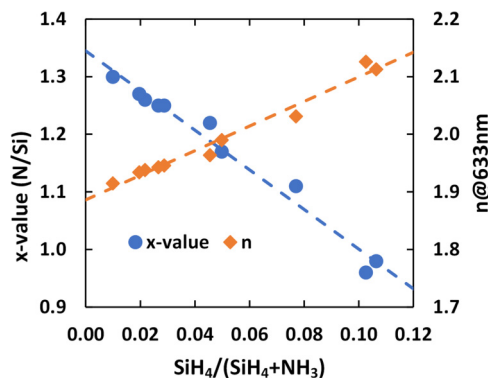


FIG. 2. Refractive index n and nitride atomic ratio N/Si as a function of the gas flow ratio $\text{SiH}_4/(\text{SiH}_4 + \text{NH}_3)$. The refractive index was measured at 633 nm with a spectroscopic ellipsometer.

40 KHz. SiH_4 and NH_3 were used as process gases to deposit the SiN_x layer. Process parameters such as gas flows and RF power were changed to produce samples with different atomic ratios of nitrogen to silicon ($x = N/Si$). The x -values were calculated from refractive index (n) values measured at 633 nm using empirical formulas.⁵ The x -value and refractive index as a function of gas flow ratio $\text{SiH}_4/(\text{SiH}_4 + \text{NH}_3)$ are shown in Fig. 2. Top oxides consisted of either PECVD deposited oxides (PDO) or plasma-assisted N_2O oxidation (PANO) layers. Bottom oxides consisted of a PDO/PANO stack. PDO or PDO/PANO stack oxides were sequentially deposited with SiN_x by an *in situ* process in the same PECVD tool without vacuum breaking. The composition of the two most relevant batches of samples is detailed in Table I.

Charge injection into the samples was achieved using a prototype plasma charging system described in more detail in a previous publication.³ The charging system uses inert gases such as nitrogen and helium to generate a plasma. The desired charges are extracted from the plasma by applying a DC bias to a sample carrier plate and injected into the ONO passivation stack. The use of inert gas ensures that the plasma does not cause parasitic film deposition or corrosion in the plasma chamber. The typical plasma charge injection conditions used on samples with our R & D prototype system³ are summarized in Table II.

The charge density in the dielectric ONO stack was determined through high-frequency (1 MHz) capacitance–voltage (C–V) measurements by a mercury probe from Materials Development

TABLE I. Different groups for charge stability tests.

Group	Bottom oxide		Nitride		Top oxide	
	Material	Thickness (nm)	Composition (x-value)	Thickness (nm)	Material	Thickness (nm)
1	PDO/PANO	20	1.01	190	PANO	4
			1.21	140		
			1.29	130		
2	PDO/PANO	19	1.32	160	PDO	15

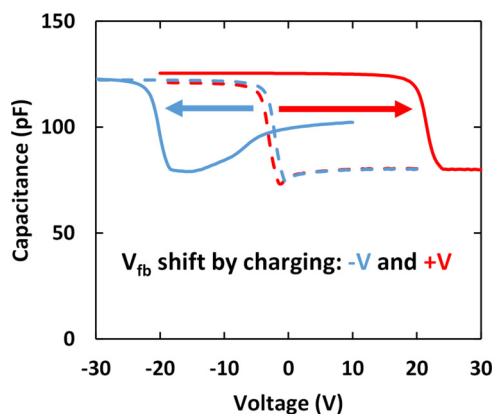
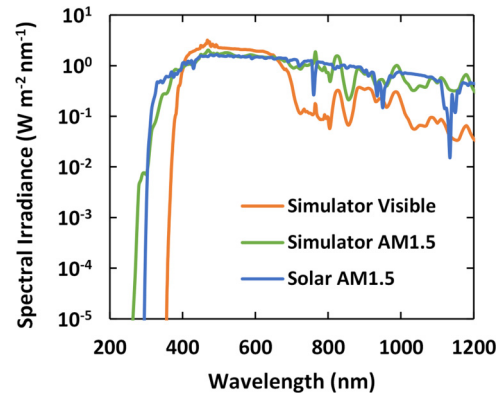
TABLE II. Plasma process conditions for negative charge injection.

N ₂ (SCCM)	Helium (SCCM)	Pressure (mTorr)	RF power (W)	DC bias (V)	Charging time (s)
30	70	300	140	80	7.6

Corporation. The use of the mercury probe allows electrical contacts on the dielectric surface without depositing metal dots.

The effect of the charging DC bias polarity on the C-V curve of the ONO stack is shown in Fig. 3. A positive DC bias results in the injection of negative charge in the form of electrons as shown by the flatband voltage shift in the positive voltage direction. A negative DC bias injects positive charge by means of positively charged ions, resulting in a flatband voltage shift in the negative voltage direction. The charge injection mechanisms are described in our earlier publication.³ For the purposes of this study, the negative charge injection was utilized. The negative charge density for this specific charge injection condition is calculated as $\sim 8.2 \times 10^{12} \text{ cm}^{-2}$, assuming a uniform charge distribution along the SiN_x layer. The actual charge density could be larger than this value because the initial injected charge is expected to be distributed more toward the surface of SiN_x.⁶

A solar simulator with a 300-W Xenon arc lamp light source manufactured by Solar Light Company, Inc. was used for light exposure tests on charged samples. The simulator produces a beam with 5 cm diameter at the sample surface. The spectral distribution of the simulator can be changed between visible light, UV, and AM1.5 through the installation of different filters and mirrors. Figure 4 compares the simulated visible light, simulated AM1.5, and actual solar AM1.5 spectra. The simulator is capable of producing a light spectrum very similar to the actual solar AM1.5 spectrum excepting for atmospheric effects at long wavelengths. For

**FIG. 3.** C-V curves before and after charge injection for injection of negative charge with positive DC bias (+V) and positive charge with negative bias (-V). For the case of positive DC bias, the injected negative charge density is $\sim 8.2 \times 10^{12} \text{ cm}^{-2}$.**FIG. 4.** Simulation light spectra provided from vendor: the visible light spectrum (orange) in comparison to the simulation AM1.5 full spectrum (green) and the actual solar AM1.5 spectrum (blue).

the simulated visible light spectrum, the main effect of the filters can be seen in the sharp drop in light intensity for sub-400 nm wavelengths (ultraviolet or UV) and reduced intensities for $>700 \text{ nm}$ wavelengths compared to the AM1.5 spectrum. Additionally, the intensity in the 400–700 nm range is slightly increased. For most tests, the visible light option was selected to represent the actual structure of solar modules where solar glass with an encapsulant buffer similarly cuts off UV light from incident sunlight. Some samples were exposed to the simulated AM1.5 light to check for any charge stability difference from visible light exposure.

Samples were exposed for up to 300 cumulative hours with C-V measurements periodically taken at five different sites near the center of the light exposure area. For most of the exposure tests, samples were placed on a hotplate set at 55°C (131°F) while under exposure to simulate field operation at high ambient temperatures like Arizona weather. Additional tests were performed on selected samples at room temperature (27°C), 66°C , and 78°C to examine the temperature dependence of the charge decay. A flatband voltage (V_{fb}) was obtained from each of the C-V curves and the average of the five values was used for the data analysis. All C-V measurements were taken at room temperature after removal of samples from the hotplate.

III. RESULTS AND DISCUSSION

Figure 5 shows V_{fb} decay curves for group 1 samples under room temperature solar simulator illumination with visible light. We characterize the flatband data above 0 V with a power law fit. Around 0 V, the V_{fb} tends to saturate, indicating the complete loss of injected negative charge. It can be seen that the decay rate drastically decreases as x-values increase. If we assume that the power law time dependence holds for positive V_{fb} , then the extrapolated flatband voltage for the $x=1.29$ sample remains above 0 V at $t=50\,000 \text{ h}$, equivalent to 25 years of field operation assuming 2000 h of vertical insolation per year in Arizona. This result indicates that the charge loss may not be related to direct loss of free

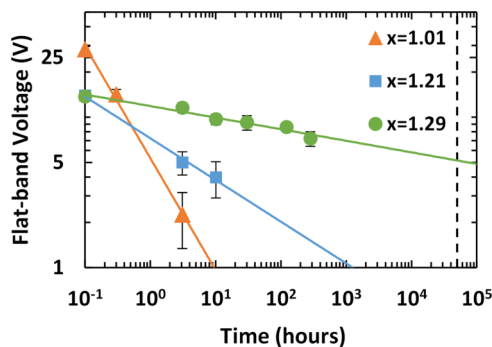


FIG. 5. V_{fb} decay curves due to charge loss by illumination of the visible light source at room temperature (27 °C) for three different x -values ($x = \text{N/Si}$ atomic ratio) of SiN_x , showing drastic improvements with increasing x -value that indicates some correlation between charge loss and SiN_x bandgap (thus, light absorption). The dotted line indicates 50 000 h. Error bars correspond to three standard deviations from the mean.

electrons going over the conduction band-offset barrier at the bottom oxide interface. The SiN_x bandgap increases with increasing x -value,⁷ and thus, the conduction band-offset barrier is expected to decrease. If free electrons were hopping over the barrier, then the decrease in barrier height would result in faster charge loss, which is the opposite of the observed trend.

In addition to the x -value of the nitride, the type of oxide used in the ONO stack was found to influence the rate of charge decay. We exposed various batches of samples to visible light at room temperature in the same manner as group 1 samples. PANO and PDO oxides were tested as both top and bottom oxides. A high-temperature thermal oxide and Al_2O_3 were also used as bottom oxides. We found that as a top oxide, PANO results in slightly slower charge decay than PDO. However, the samples with PDO top oxides had higher initial V_{fb} when charged, which offsets the higher decay. In addition, we found that PANO is not suitable as a top oxide because it led to poor cell performance when applied to bifacial PERC cells. We also evaluated a PANO layer as a bottom oxide and found its thickness saturates at about 4 nm, which is too thin to hold injected negative charge. Comparing the thermal oxide and PDO as bottom oxides, we observed similar charge decay rates for the two despite the higher film quality of the thermal oxide. Finally, we tested a PDO/PANO stack as a bottom oxide. This stack was found to be better than a PDO alone because the underlying PANO improves the thickness uniformity of the subsequently deposited PDO. The PANO also produces a higher quality interface than the PDO. This was confirmed by greater stretching out of C–V curves for the PDO oxide, which indicates the presence of more deep interface states than for the PANO oxide. The PDO/PANO stack would still be more cost-effective than a high-temperature oxide because the oxides are subsequently deposited by an *in situ* PECVD at low temperature without vacuum breaking.

The behavior of samples with Al_2O_3 bottom oxides differed from other tested samples, demonstrating a slow increase in V_{fb}

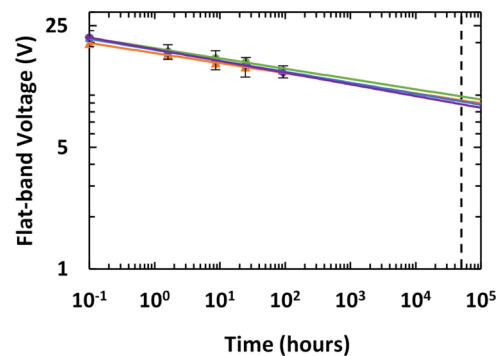


FIG. 6. Power law fit for test of optimized group (group 2) under visible light at 55 °C. Four samples were tested, each represented by a different colored shape and line. Error bars correspond to three standard deviations from the mean.

with exposure time. This increase may be due to charge redistribution toward the bottom oxide. It has also been shown that UV irradiation of Al_2O_3 can produce an increase in fixed charge density due to photo-injection of electrons from Si into Al_2O_3 .⁸ Under sample test conditions, the UV component is a very small portion of the light spectrum used for illumination, and electron injection from the substrate is against the internal electric field formed by the negative charge in Al_2O_3 . These factors make it likely that charge redistribution is the primary cause of the V_{fb} increase for the Al_2O_3 sample. However, the small remaining UV component could nonetheless increase the negative fixed charge present in Al_2O_3 over long exposure times.⁹

After a series of ONO stack recipe experiments, we found an optimum ONO stack that gives the best results in terms of both charge stability and cell performance. The samples with the optimized ONO stack are denoted as group 2 samples in Table I. These optimized samples were exposed to visible light at a temperature of 55 °C. The result of the charge stability test on a set of the samples is shown in Fig. 6, with decay trends fit to a power law. The extrapolated flatband voltage remains 9.3 ± 0.5 V at 50 000 h, corresponding to a negative charge density of $(3.6 \pm 0.4) \times 10^{12} \text{ cm}^{-2}$ calculated with the assumption of a uniform charge distribution through the SiN_x layer. This assumption is reasonable because the initial non-uniform distribution of injected charge toward the SiN_x surface is expected to rapidly approach a uniform distribution during light exposure with free electrons and holes generated by illumination.

From the results of charge stability tests, we determined possible mechanisms for charge loss. The most striking result in the group 1 test is the strong dependence of decay on the x -value of silicon nitride. It is well known that for PECVD SiN_x , the bandgap of the material increases with increasing x -value.⁷ Higher bandgaps result in reduced light absorption, which, in turn, results in a lower electron–hole pair generation rate.

To explore the relation between the V_{fb} decay and electron–hole generation rate, the generation rate in SiN_x near the nitride/bottom oxide interface was calculated as a function of the nitride

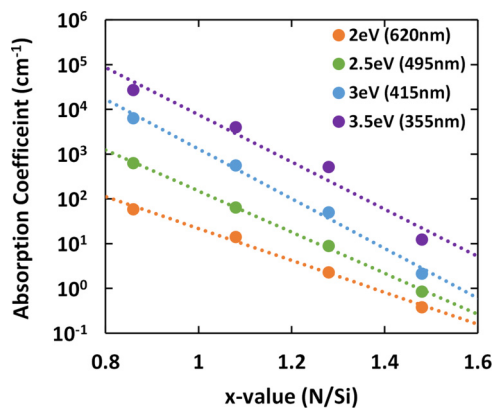


FIG. 7. Absorption coefficient of SiN_x vs x -value for select photon energies. The dotted lines serve as a guide to the eye.

x -value. The formula for the electron-hole pair generation rate is

$$G = \alpha N_o e^{-\alpha d}, \quad (1)$$

where α is the absorption coefficient, N_o is the photon flux at the surface of the sample, and d is the distance into the sample.

The absorption data were obtained from published data of the absorption coefficient of SiN_x as a function of photon energy for samples encompassing a wide range of x -values.¹⁰ These data were used to obtain the absorption coefficient as a function of x -value, as shown in Fig. 7, for several photon energies in the visible light range. The photon flux was obtained from the visible light spectrum as shown in Fig. 4. The distance in the nitride was set as 10 nm from the bottom oxide interface. Generation rates were calculated for every 1 nm between 380 and 700 nm and summed to obtain the overall generation rate. The absolute value of the power law exponents were taken to represent V_{fb} decay, with larger exponents indicating faster decay. Figure 8 shows the correlation

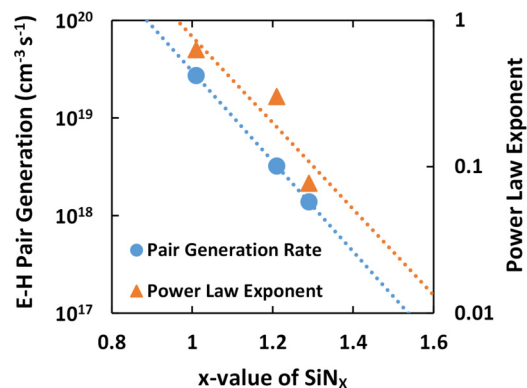


FIG. 8. Electron-hole pair generation and power law exponent under visible light as a function of x -value of SiN_x . The dotted lines serve as a guide to the eye.

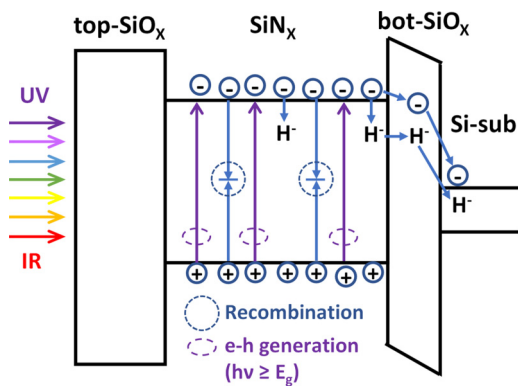


FIG. 9. Schematic band diagram for the ONO passivation stack, showing light-associated dynamics in SiN_x , including electron-hole (e)-(h) pair generation, recombination, electron-capturing hydrogen (H^-), and some possible charge loss mechanisms (electron transport and/or H^- transport through bottom oxide).

between the power law exponent and calculated electron-hole pair generation rate as a function of the SiN_x x -value. The general trend of the two suggests that the V_{fb} decay may be related to photo-generated free electrons.

The light-associated dynamics in SiN_x and two possible charge loss mechanisms are depicted in Fig. 9. These mechanisms are as follows:

- (1) Photo-generated electrons are lost through hopping transport between trap centers through the bottom oxide to the substrate.
- (2) Negatively charged hydrogen (H^-) diffuses through the nitride and bottom oxide to the substrate.

Our oxide tests cast doubt on the possibility of the mechanism (1). For this mechanism, the rate of charge loss would be dependent on the density of trap centers available for electron hopping. However, we found that in terms of bottom oxide both thermal oxide and PDO demonstrated similar V_{fb} decay trends despite the much higher trap densities in the PDO. Based on this observation and considering Al_2O_3 as an effective barrier to hydrogen diffusion,¹¹ we propose that mechanism (2) is the probable mechanism responsible for the loss of photo-generated electrons.

To further expand on mechanism (2), we note that it is a three-step process. In SiN_x after firing, a hydrogen-depleted region is generated near the bottom oxide because hydrogen near the bottom oxide is known to diffuse to the silicon substrate during high-temperature firing. In the first step of the process, hydrogen atoms diffuse through the hydrogen depletion region in SiN_x toward the bottom oxide. Next, some of the hydrogens arriving at the bottom oxide capture an electron, which is a relatively fast process because abundant photo-generated electrons are available for capturing. Finally, the negatively charged hydrogens move fast through the bottom oxide to the substrate. It is well known in the silicon Metal-Oxide-Silicon (MOS) technology that a degradation of MOSFET by negative bias temperature stress (NBTS) is related to the movement of charged hydrogen in the gate oxide (SiO_2) at

elevated temperatures with a very low activation energy around 0.05 eV.^{12,13} The hydrogen diffusion in SiN_x of the three consecutive steps must be the slowest one and thus the rate limiting step in the charge loss process.

The power-law behavior of the flatband voltage seen in group 1 and group 2 samples is indicative of dispersive hydrogen diffusion through the nitride. Dispersive transport has been observed in a wide variety of amorphous materials. Initially observed in electronic transport, dispersive transport was later found in atomic diffusion as well.¹⁴ Dispersive behavior is characterized by a power law dependence of a parameter such as mobility on time. The general form of the time dependence is $t^{-\beta}$, where t is time and β is the dispersion parameter that ranges from 0 to 1. While dispersive transport is common to amorphous materials, the values of the dispersion parameter are material dependent and can be strongly affected by fabrication and processing conditions. Atomic dispersive transport analogous to electron dispersion was first documented by Kakalios *et al.*¹⁴ who found a dispersion parameter around 0.2–0.25 for the diffusion coefficient of atomic hydrogen in boron-doped a-Si:H annealed at 200 °C. Various groups of researchers investigated dispersive transport of hydrogen in undoped a-Si:H for different deposition temperatures as well as for post-deposition annealing temperatures with a wide range of dispersion parameters from 0.23 to 0.75.^{15–17} In addition to atomic hydrogen, dispersive transport of molecular and charged hydrogen has been studied in materials such as amorphous SiO₂.¹⁸

We have obtained dispersion parameter (β) values of 0.062 ± 0.005 from the fitting of group 2 V_{fb} decay at 55 °C under visible light. Atomic and ionic hydrogen diffusion are expected to be much slower in SiN_x than a-Si:H,^{19,20} explaining the smaller dispersion parameter value found in our samples compared to those in a-Si:H.

We confirmed the validity of the test conditions with additional exposure tests utilizing different conditions. Concurrently with these tests, samples of various compositions were stored in the dark at room temperature and periodically measured over the course of several months. The stored samples showed CV

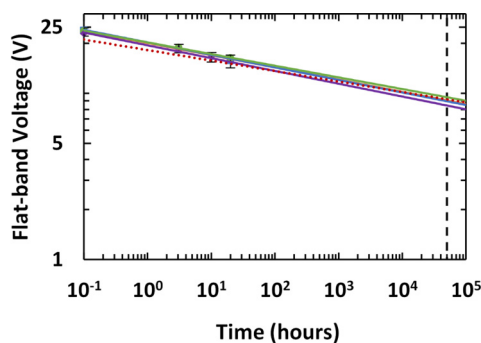


FIG. 10. Power law fit for V_{fb} decay under AM1.5 exposure at 55 °C (solid lines). A typical case of V_{fb} decay under visible light at 55 °C is shown for comparison (dotted red line).

TABLE III. Average dispersion parameter (β) and flatband voltage (V_{fb}) at 50 000 h for visible light and AM1.5 exposure at 55 °C.

Visible (55 °C)		AM1.5 (55 °C)	
β	V_{fb}	β	V_{fb}
0.062 ± 0.005	9.3 ± 0.5	0.074 ± 0.004	9.0 ± 0.5

measurements with consistent V_{fb} , verifying that any measured changes in the V_{fb} of samples are induced by light and heat exposure.

In one set of tests, the solar simulator was set up to simulate the AM1.5 spectrum while the hotplate temperature was maintained at 55 °C. The V_{fb} decay of group 2 samples under AM1.5 exposure fit to a power law trend is shown in Fig. 10. A typical visible light decay curve, adapted from Fig. 6, is also included for comparison. The corresponding dispersion parameters and extrapolated V_{fb} at 50 000 h for both visible light and AM1.5 are shown in Table III. The AM1.5 decays are slightly faster than the visible light tests, probably due to the increased electron–hole pair generation rate caused by the UV component of the AM1.5 spectrum. However, the V_{fb} at 50 000 h is still 9.0 ± 0.5 V, which corresponds to a charge density of $(3.5 \pm 0.4) \times 10^{12} \text{ cm}^{-2}$. As noted earlier, in an actual solar module, most of the UV component will not reach the cell, so the AM1.5 exposure represents the worst possible spectrum of light exposure.

Additional visible light tests were performed on group 2 samples at 55, 66, and 78 °C. The results at 55 and 78 °C are shown in Fig. 11 and Table IV. The trends suggest an increase in dispersion parameter with increased temperature, which would match the findings of other groups.¹⁷ This is accompanied by a reduced V_{fb} at 50 000 h. The 55 °C extrapolated V_{fb} at 50 000 h is ~ 10.8 V, while at 78 °C, the extrapolated V_{fb} is ~ 9.9 V, corresponding to charge densities of $\sim 4.2 \times 10^{12}$ and $\sim 3.9 \times 10^{12} \text{ cm}^{-2}$, respectively. It should be noted that these samples were discharged and then recharged with standard conditions prior to testing. We found that this results in a slightly higher V_{fb} than samples charged once. However, the

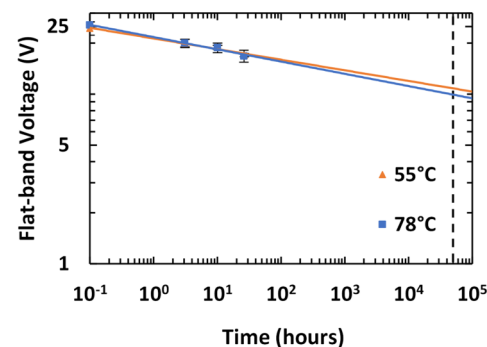


FIG. 11. V_{fb} decay under visible light at 55 and 78 °C fit to a power law trend.

TABLE IV. Dispersion parameter (β) and flatband voltage (V_{fb}) at 50 000 h for visible light exposure at 55 and 78 °C.

Visible (55 °C)		Visible (78 °C)	
β	V_{fb}	β	V_{fb}
~ 0.063	~ 10.8	~ 0.072	~ 9.9

general decay trend is not affected as evinced by the dispersion parameter at 55 °C matching previous tests.

IV. CONCLUSIONS

We have demonstrated the charge stability of an ONO stack with negative charge injected by plasma charging technology. Different recipes for each of the ONO layers were tested by exposure to visible and AM1.5 light at temperatures ranging from 55 to 78 °C. The dispersive diffusion of negatively charged hydrogen through nitride was found to be the most probable mechanism of charge loss in the tested samples. An optimized stack was fabricated with PDO/PANO bottom oxide, PDO top oxide, and SiN_x with an x-value of 1.32 that maintained similar decay characteristics in all tested conditions. Based on the hypothesis of dispersive hydrogen transport, the stack is predicted to retain a negative charge density of $(3.6 \pm 0.4) \times 10^{12} \text{ cm}^{-2}$ after 50 000 h of operation in environments with high ambient temperature such as Arizona. This ensures that the stack remains capable of providing field-effect passivation through the formation of an accumulation layer under one sun illumination. The stability of the negative charge makes the plasma charge injection technology a viable low-cost alternative to the current Al₂O₃ technology.

ACKNOWLEDGMENTS

This material was based upon work supported by the U.S. Department of Energy's Office of Energy Efficiency and Renewable Energy (EERE) under the Solar Energy Technologies Office Award No. DE-EE0008566. The views expressed herein do not necessarily represent the views of the U.S. Department of Energy or the United States Government.

AUTHOR DECLARATIONS

Conflict of Interest

The authors have no conflicts to disclose.

Author Contributions

Christopher Chen: Data curation (lead); Formal analysis (lead); Investigation (lead); Writing – original draft (lead). **Jeong-Mo**

Hwang: Conceptualization (lead); Funding acquisition (lead); Methodology (lead); Project administration (lead); Resources (lead); Supervision (lead); Writing – review & editing (lead). **Young-Woo Ok:** Methodology (supporting); Project administration (supporting). **Wook-Jin Choi:** Data curation (supporting); Formal analysis (supporting). **Vijaykumar Upadhyaya:** Resources (supporting). **Brian Rounsaville:** Resources (supporting). **Ajeet Rohatgi:** Funding acquisition (supporting); Supervision (supporting).

DATA AVAILABILITY

The data that support the findings of this study are available from the corresponding author upon reasonable request.

REFERENCES

- B. Hoex, S. B. S. Heil, E. Langereis, M. C. M. van de Sanden, and W. M. M. Kessels, *Appl. Phys. Lett.* **89**, 042112 (2006).
- S. Dauwe, L. Middlestadt, A. Metz, and R. Hezel, *Prog. Photovoltaics Res. Appl.* **10**, 271 (2002).
- J.-M. Hwang, *J. Appl. Phys.* **125**, 173301 (2019).
- J.-M. Hwang, C. Chen, Y.-W. Ok, W. Choi, A. Upadhyaya, V. Upadhyaya, B. Rounsaville, and A. Rohatgi, in *Proceedings of 48th IEEE Photovoltaic Specialist Conference* (IEEE, New York, 2021), p. 2119.
- E. Bustarret, M. Bensouda, M. C. Habrard, J. C. Bruyère, S. Poulin, and S. C. Gujrahi, *Phys. Rev. B* **38**, 8171 (1988).
- K. H. Min, J.-M. Hwang, E. Cho, H. Song, S. Park, A. Rohatgi, D. Kim, H.-S. Lee, Y. Kang, Y.-W. Ok, and M. G. Kang, *Prog. Photovoltaics* **29**, 54 (2021).
- J. Robertson, *Philos. Mag. B* **69**, 307 (1994).
- R. Hezel and K. Jaeger, *J. Electrochem. Soc.* **136**, 518 (1989).
- B. Veith-Wolf, R. Witteck, A. Morlier, H. Schulte-Huxel, M. R. Vogt, and J. Schmidt, *IEEE J. Photovoltaics* **8**, 96 (2018).
- J. Kanicki, W. L. Warren, C. H. Seager, M. S. Crowder, and P. M. Lenahan, *J. Non-Cryst. Solids* **137&138**, 291 (1991).
- L. Helmich, D. C. Walter, D. Bredemeier, and J. Schmidt, *Phys. Status Solidi RRL* **14**, 2000367 (2020).
- S. A. Sheikholeslam, H. Manzano, C. Grecu, and A. Ivanov, *J. Mater. Chem. C* **4**, 8104 (2016).
- L. S. Morrissey, D. Pratt, W. M. Farrell, O. J. Tucker, S. Nakhla, and R. M. Killen, *Icarus* **379**, 114979 (2022).
- J. Kakalios, R. A. Street, and W. B. Jackson, *Phys. Rev. Lett.* **59**, 1037 (1987).
- J. Shinar, R. Shinar, S. Mitra, and J.-Y. Kim, *Phys. Rev. Lett.* **62**, 2001 (1989).
- X.-M. Tang, J. Weber, Y. Baer, and F. Finger, *Phys. Rev. B* **41**, 7945 (1990).
- X.-M. Tang, J. Weber, Y. Baer, and F. Finger, *Physica B* **170**, 146 (1991).
- T. Grasser, W. Göss, and B. Kaczer, *IEEE Trans. Device Mater. Rel.* **8**, 79 (2008).
- G. C. Yu, *J. Mater. Chem.* **13**, 841 (2003).
- G. C. Yu and S. K. Yen, *Appl. Surf. Sci.* **201**, 204 (2002).